UC San Diego
UC San Diego Previously Published Works

Title

MilliMirror

Permalink

https://escholarship.org/uc/item/56p8b312

Authors

Qian, Kun

Yao, Lulu

Zhang, Xinyu

et al.

Publication Date

2022-10-14

DOI

10.1145/3495243.3517024

Peer reviewed

MilliMirror: 3D Printed Reflecting Surface for Millimeter-Wave Coverage Expansion

Kun Qian, Lulu Yao, Xinyu Zhang, Tse Nga Ng
University of California San Diego

ABSTRACT

Next generation wireless networks embrace mmWave technology for its high capacity. Yet, mmWave radios bear a fundamental coverage limitation due to the high directionality and propagation artifacts. In this paper, we explore an economical paradigm based on 3D printing technology for mmWave coverage expansion. We propose MilliMirror, a fully passive metasurface, which can reshape and resteer mmWave beams to anomalous directions to illuminate the coverage blind spots. We develop a closed-form model to efficiently synthesize the MilliMirror design with thousands of unit elements and across a wide frequency band. We further develop an economical process based on 3D printing and metal deposition to fabricate MilliMirror. Our field test results show that MilliMirror can effectively fill the coverage holes and operate transparently to the standard mmWave beam management protocols.

CCS CONCEPTS

• **Hardware** → **Wireless devices**; **Analysis and design of emerging devices and systems**; • **Networks** → **Network experimentation**.

KEYWORDS

Intelligent Reflecting Surface, Smart Surface, Metasurface, Metamaterial, Millimeter-wave Networks, 5G, 6G, Phased Array Signal Processing, 3D Printing

1 INTRODUCTION

Millimeter-wave (mmWave) technology has long been advocated as a cornerstone for 5G and beyond, and has recently been deployed by major carriers worldwide [2]. Stepping into the mmWave territory is an inescapable long-term choice for wireless operators, due to the exponential growth of mobile data and the pressing spectrum crunch at the low-frequency bands. Thus the standardization portfolio of mmWave keeps expanding in recent years, including
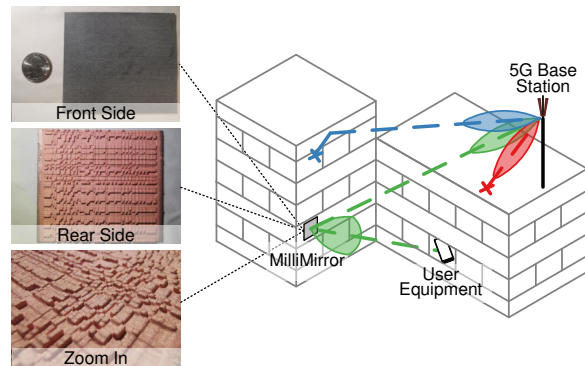
Figure 1: MilliMirror and one of its representative use case, the outdoor-to-indoor coverage expansion.

not only the 5G cellular broadband on the 20-40 GHz spectrum, but also WiGig (802.11ad/ay) on the 57-71 GHz band, and will likely expand to above 100 GHz in the forthcoming 6G era [28].

Despite their exciting prospects, the spotty coverage remains a fundamental barrier that hinders the pervasive use of mmWave technologies. Recent measurement [39] shows that mmWave 5G connection appears less than 1% of the time on average across carriers in the US. Complicating things further, traditional outdoor-to-indoor coverage is almost impossible with mmWave, particular for modern buildings in urban canyon environment. These problems are just a precursor to the beyond-5G (B5G) era where spectrum use may move to the sub-Terahertz bands [28] with higher directionality and worse propagation artifacts.

In this paper, we propose MilliMirror, a 3D printed metasurface, as a new paradigm to tackle the mmWave coverage problem. MilliMirror does not generate mmWave signals by itself. Instead, it can reflect mmWave signals towards *anomalous directions* that do not comply with the Snell's laws, and even reshape the signals into a variety of beam patterns, hence overcoming the intrinsic propagation artifacts and illuminating the coverage blind spots. Unlike active relays [1, 18, 43] or digitally controlled reflectarrays [9, 54], MilliMirror has no electronic components or ICs, and can be mass fabricated through ordinary 3D printing processes at extremely low cost. Owing to a thin form factor, it can be attached on the facades of ambient environment such as buildings, walls, advertisement boards, *etc.* Fig. 1 demonstrates a representative use case of MilliMirror. Due to the blockage of LoS and lack of (or weak) multipaths from natural reflectors, signals from the outdoor mmWave base station (BS) cannot reach the indoor user equipment (UE). By placing MilliMirror nearby to reflect and refocus the mmWave beam, a strong NLoS path can be created. Thanks to the reciprocity of the channel, MilliMirror can facilitate both the uplink and downlink of mmWave networks. It is transparent to the standard beam management protocols, so no modifications or intervention to the existing mmWave devices are needed.

MilliMirror uses a large array of sub-wavelength "unit element" reflectors to form a metasurface. The most crucial design choice for MilliMirror lies in the type of the unit reflector and the mechanism to tune the reflection coefficients so as to create a desired beamforming effect. We use a tiny rectangular cuboid, made of dielectric material and backed by a thin metal layer, as a unit element. Such a metal-backed dielectric cuboid (MBDC) structure is easy to fabricate and leads to a closed-form model of the reflection coefficient. By tuning the thickness of the MBDC, different phase shifts ranging from $0°$ to $360°$ can be applied on the reflection signal. Packing thousands of such unit reflectors with different phase shifts, MilliMirror is endowed with the capability of adjusting the reflection signal power to any direction and thus resteering the signals towards non-Snell's directions in general.

To create an objective reflection beam pattern (e.g., the green beam in Fig. 1), we need to search the phase shift configurations across thousands of unit elements. Existing pattern synthesis algorithms, such as iterative Fourier transform [12] and differential evolution algorithm [15], use parametric objective patterns, heuristic objective functions and opportunistic searching strategies. Though applicable for traditional phased arrays, they converge slowly and are very likely to end up with poor solutions in a huge searching space like MilliMirror. To overcome this challenge, we design a new *reflection beam synthesis algorithm*, which transforms the objective pattern based on the power conservation between the incident and reflection signals. The transformation establishes a closed-form relation between the objective and the phase shifts, thus enabling rapid convergence. An additional challenge is that the MBDCs can only modulate the phase, not magnitude, of incident signals, which inevitably results in nulls in the reflected main lobe. Our algorithm overcomes this hindrance by approximating and decomposing the 2D (azimuth and elevation angles) pattern synthesis into two orthogonal 1D processes, which can efficiently generate smooth patterns.

Whereas the basic MilliMirror model assumes single carrier signals, the desired phase shifts deviate from the model over a wider bandwidth. This in turn distorts the desired beam pattern especially for large surfaces. To overcome this challenge, we develop a model to decouple the size and the bandwidth of MilliMirror, and upgrade the pattern synthesis so it becomes frequency independent. The size of MilliMirror can thus be scaled up to increase the reflection gain, without limiting the signal bandwidth.

Finally, it is not straightforward to turn the ideal MilliMirror model into a fabricatable metasurface. We have tested various recipes and finally adopt a 3D printing technique (i.e., Multi Jet Fusion) to fabricate the dielectric cuboids, and a two-step deposition technique (i.e., sputtering and electroplating) to coat a copper layer. MilliMirror has a significantly lower cost compared with PCB fabricated reflectarray antenna. For example, compared with a patch antenna array with similar size and gain, the cost of MilliMirror is lower by at least an order of magnitude (Sec. 5).

We have fabricated MilliMirror samples with a variety of sizes, ranging from 64×64 to 128×128 unit elements per surface. We further conducted extensive field experiments with commercial 802.11ad devices to verify the MilliMirror design. Our experiments show that MilliMirror can accurately generate objective

patterns to cover the blind spots, operate transparently to the standard beam management protocols, and can be applied to overcome various NLoS scenarios such as the outdoor-to-indoor, the around-the-corner, and self-blockage due to misorientation. While the experiments are conducted for 60 GHz frequencies, the model-driven design of MilliMirror is readily available to mitigate the coverage problems of other frequency bands.

In summary, the main contributions of MilliMirror are:

(i) We design MilliMirror, a passive chipless metasurface that resteers and reshapes incident signals with arbitrary reflection patterns. Our design is driven by a closed-form model and a novel pattern synthesis algorithm.

(ii) We develop a novel model that decouples the size and the bandwidth of MilliMirror, so as to strike a balance between reflection beamforming gain and signal bandwidth.

(iii) We propose a fabrication process for MilliMirror based on 3D printing and metal coating, which allows for rapid mass production. Our experiments verify the feasibility and usefulness of MilliMirror in mmWave coverage expansion. Whereas our case studies focus on mmWave networking scenarios, MilliMirror can be easily used to facilitate NLoS sensing, such as around-the-corner radar and whole home activity recognition.

2 RELATED WORK

RF metasurfaces. RF metasurfaces are artificial surface structures that can abruptly change the amplitude/phase of incident electromagnetic waves. With different reflection and refraction properties, they can harvest RF energy [4, 56] or resteer the signals [6, 9, 25, 54]. A metasurface usually consists of many similar unit elements, such as textured 2D patches [22, 34, 38, 46], inductive/capacitive resonators [9, 21], metallic grating structures [13, 27], etc. One or more hardware parameters (e.g., geometries of ring patches [19] or voltage applied on varactors [9]) are used to control the amplitude/phase discontinuities of individual elements which together create superimposed radiation patterns.

However, it is challenging to apply existing metasurface designs to the mmWave bands. On one hand, existing RF metasurface elements have complex electromagnetic artifacts such as mutual coupling. Their reflection properties do not bare a closed-form relation with the element parameters (e.g., geometrical layout). To form a target beam pattern, they have to search across each parameter dimension with wave-level simulation [45], which becomes challenging for a mmWave metasurface with hundreds to thousands of elements. In contrast, MilliMirror adopts 3D metal-backed dielectric elements with a simple structure and a closed-form model, based on which the pattern synthesis for arbitrarily large sizes can be easily derived. On the other hand, existing metasurfaces require PCB fabrication, which can be very expensive for mmWave due to the specialized substrate and strict fabrication tolerances for parts like transmission lines and vias. In contrast, MilliMirror is fabricated using commodity 3D printers, which lowers the cost by at least an order of magnitude (Sec. 5). This can be a crucial advantage particularly for facilitating the 5G mmWave deployment which would otherwise need high density basestations and hence high cost for pervasive coverage. In [44], a 3D printed metasurface tunable with fluids is proposed. However, limited by the routing of fluidic channels, this design can only generate 1D beamforming

patterns. Moreover, water has a high tangent loss and leads to high loss due to the absorption of millimeter-wave signals.

Wireless smart surfaces. Smart surfaces [5, 11, 16, 36, 54, 64, 65] have been developed in recent years to artificially manipulate wireless channels and extend the network coverage. For example, LLAMA [11] rotates the polarization of desired signal to isolate it from interference. RFocus [5] uses a large antenna array to improve the SNR of reflected or pass-through WiFi signals. Though reconfigurable at runtime, these smart surfaces rely on an active digital circuit to control the elements, and require real-time channel measurements as input to make the control decisions. Several systems [11, 16] assume a wireline control channel between the smart surfaces and the Tx/Rx which constrains the practical deployment. Other works propose channel measurement based approach to select the reflection beam [5, 54]. However, due to lack of synchronization with the Tx, these surfaces can hardly follow the rapid beam switching (*e.g.*, 125 *μs* per beam for 5G [20]). In contrast, MilliMirror represents an alternate solution to mmWave coverage problems. It resteers the signals to cover a fixed blind spot or a wide area. Although configurable only at design time, it is fully passive and does not require coordination with existing Tx/Rx.

Smart surfaces have also been used to convey information and enhance radar sensing [35, 37, 50]. Millimetro [50] modulates incident FMCW chirps to encode identity of the target. RoS [37] encodes information with the joint RCS pattern of a passive array of retroreflective arrays. MilliMirror can benefit mmWave sensing in an orthogonal way by extending its coverage and enhancing its performance in NLoS.

3D printing for RF. Recently, 3D printing has extended from the conventional polymer to general materials. 3D printed RF components have also been enabled as economic replacement of PCB fabrication, such as lenses [63], reflectarray [10], waveguides [17], transmission lines [14], *etc.* With a similar purpose as MilliMirror, WiPrint [62] prints metallic reflectors with specially designed shapes and co-locate them with a WiFi Tx to customize indoor coverage. It essentially acts as part of the Tx to reshape its antenna patterns, yet it cannot extend the coverage to fully blocked regions where no multipath is attainable. In contrast, MilliMirror is deployed in the far field of the Tx/Rx, and can reflect directional beam patterns towards fully blocked regions.

Expanding mmWave coverage. Passive metallic reflectors have been explored for long distance satellite or cellular communications [31, 42, 51]. Yet such reflectors only create specular reflections with limited angular field-of-view (FoV), and the beam direction is confined by the poses of reflectors. It is well known that a mmWave phased array itself can only switch beams within a limited FoV (typically narrower than 90°). The FoV can be expanded by using an array of phased arrays [57], or through coordination among multiple base stations [59]. But these solutions cannot overcome the coverage holes. By sensing ambient reflectors's position/orientation/RCS and placing the mmWave basestations judiciously [60], it is feasible to mitigate the patchy coverage, yet the effectiveness highly depends on the ambient environment. Alternatively, a mmWave relay [1, 18, 43] can boost the mmWave coverage and improve link robustness. However, it is questionable whether it will become a scalable solution, considering the high implementation cost due to hardware complexity, power consumption, *etc.*
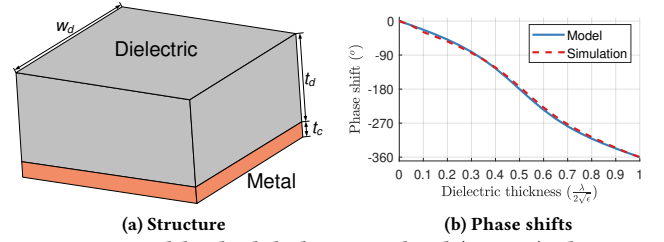

(a) Structure   (b) Phase shifts

Figure 2: Metal-backed dielectric cuboid (MBDC), the unit element of MilliMirror.

3 MILLIMIRROR MODEL

In this section, we present the basic design of MilliMirror, including the phase model of the unit element and the reflection beam pattern synthesis algorithm.

3.1 Phase Model of the Unit Element

MilliMirror uses the metal-backed dielectric cuboid (MBDC) as the unit element, which is easy to fabricate and lead to a closed-form phase model, as we will elaborate on shortly. As illustrated in Fig. 2a, a MBDC has a simple structure, with a thick dielectric cuboid on top and a thin metallic layer on the bottom. The thickness of the dielectric cuboids varies across different MBDC elements, but they all share the same top which forms a flat dielectric surface. When thousands of such MBDCs are placed tightly together, the corresponding metasurface looks like a dielectric slab with a flat top but many rectangular "stacks" etched on the bottom, as shown in Fig. 4. Intuitively, *the incidental signals penetrate the dielectric cuboids with different thickness (and hence different impedance) before hitting the bottom metal layer, which causes different levels of phase distortion.*

The phase distortion can be characterized by the complex reflection coefficient Γ at the top surface of the dielectric cuboid, where signals enter/leave the MBDC. Intuitively, Γ describes how much of a wave is reflected by the impedance discontinuity between the transmission medium (*e.g.*, the air vs. the dielectric substrate). Γ is formally defined as the ratio of the complex amplitude of the reflected wave to that of the incident wave [26], and can be characterized by the surface impedance of the dielectric surface [8]:

$$\Gamma = \frac{Z_s - RZ_0}{Z_s + RZ_0}, \tag{1}$$

where Z_s is the normal impedance (in the unit of Ω per unit area) of the dielectric surface. $Z_0 = 120\pi$ Ω is the impedance of free space, and $R = \frac{1 - \sin^2 \phi \sin^2 \theta}{\cos \theta}$ is a coefficient that depends on the azimuth ϕ and elevation θ of the incident signal relative to the dielectric surface, as shown in Fig. 3a.

Given the approximately lossless dielectric material, the normal impedance Z_s of the MBDC is pure reactance [8]:

$$Z_s = \frac{jZ_0}{\sqrt{\epsilon}} \tan \frac{2\pi\sqrt{\epsilon}}{\lambda} t_d, \tag{2}$$

where ϵ is the dielectric constant of the cuboid, and λ is the wavelength of the incident signal in free space. t_d is the thickness of the cuboid, *i.e.*, the distance between the top dielectric surface and the bottom metal layer. Given that the impedance of free space is pure resistance, the *complex reflection coefficient* of the MBDC can be represented as:
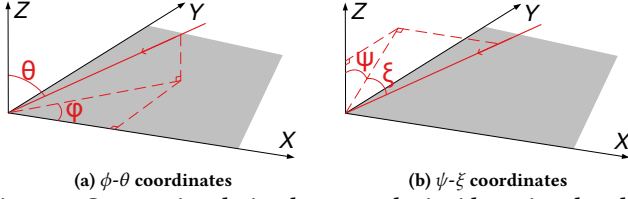
(a) ϕ-θ coordinates   **(b) ψ-ξ coordinates**

Figure 3: Geometric relation between the incident signal and the top dielectric interface of the MBDC.

$$\Gamma = e^{-j2\arctan\frac{1}{R\sqrt{\epsilon}}\tan\sqrt{\epsilon}kt_d} \tag{3}$$

Theoretically, when the thickness of the dielectric cuboid varies from 0 to $\frac{\lambda}{2\sqrt{\epsilon}}$, the phase shift to the incident signal also varies from 0 to 2π. This *effectively enables the MBDC to act as a phase shifter with respect to the incident signal.*

To verify this model, we construct a MBDC in the Ansys HFSS 3D electromagnetic field simulator, and create an incidental plane wave along its broadside direction, *i.e.*, perpendicular to its top surface. Fig. 2b shows that the theoretical phase shifting as a function of the MBDC thickness matches the full wave simulation well.

By packing thousands of MBDC elements, we create a MilliMirror metasurface with a closed-form *reflection pattern*. Specifically, suppose MilliMirror consists of $N \times N$ MBDCs with side length w_d, the phase shift of the MBDC elements at the k-th row and the l-th column is $\varphi_{k,l}$, and the azimuth and elevation angle of the incident signal is ϕ_i and θ_i. The corresponding *reflection gain* towards the azimuth angle ϕ_r and elevation θ_r is:

$$F_{\phi_r,\theta_r} = \sum_{k,l=-N/2}^{N/2-1} \sqrt{\sigma_0}e^{j\varphi_{k,l}} \cdot e^{j\frac{2\pi}{\lambda}\vec{p}_{k,l}^T\vec{e}_i} \cdot e^{j\frac{2\pi}{\lambda}\vec{p}_{k,l}^T\vec{e}_r}, \tag{4}$$

where $\vec{e} = (\cos\phi\sin\theta, \sin\phi\sin\theta, \cos\theta)^T$ is the unit direction vector of the signal, $\vec{p}_{k,l} = (kw_d, lw_d, 0)^T$ is the location vector of the element at the k-th row and l-th column, and σ_0 is the reflection gain of a single MBDC, which is estimated via full-wave simulation. The term $e^{j\frac{2\pi}{\lambda}\vec{p}_{k,l}^T\vec{e}_i}$ represents the phase delay introduced by different propagation distances when the signal approaches different MBDCs. The term $e^{j\frac{2\pi}{\lambda}\vec{p}_{k,l}^T\vec{e}_r}$ is the phase delay introduced by different propagation distances of the signal reflected by MBDCs. Thus, *by controlling the thickness of the MBDCs, the metasurface can have certain distribution of phase shifts and thus form different reflection beam patterns.*

3.2 Reflection Pattern Synthesis

MilliMirror aims to create signal paths between a BS and the blocked regions. For ease of exposition, we assume the blind spots can be covered by a beam with certain beam width, so we represent the *objective beam pattern* by specifying the direction and width of the beam in 2D polar coordinates. But general patterns such as pencil beam and multi-arm beam follow the same synthesis method. Denote the objective reflection beam pattern of MilliMirror as $\tilde{F}_{\phi_r,\theta_r}$. *The goal of our reflection pattern synthesis algorithm is to find the set of phase shifts $\varphi_{k,l}$ for the MBDC elements, so that the actual pattern F_{ϕ_r,θ_r} approaches the objective $\tilde{F}_{\phi_r,\theta_r}$, i.e.,*

$$\varphi_{k,l} = \text{argmin}_{\varphi_{k,l}} \sum_{\phi_r,\theta_r} (|F_{\phi_r,\theta_r}|^2 - |\tilde{F}_{\phi_r,\theta_r}|^2)^2. \tag{5}$$

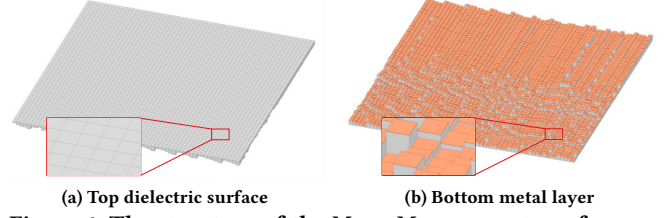**(a) Top dielectric surface**   **(b) Bottom metal layer**

Figure 4: The structure of the MilliMirror metasurface.

Standard beam pattern synthesis algorithms for phased arrays, such as iterative Fourier transform [12] and differential evolution algorithm [15], use the variants of Eq. (5) as the objective functions. However, these algorithms are not guaranteed to generate near-optimal patterns. *First*, these algorithms usually normalize the objective patterns by the *main lobe level (MLL)* and use the power delta between the MLL and the side lobe level (SLL) to characterize the objective. However, determination of the power delta relies on heuristics. If it is too small, the MLL of the resulting pattern is not maximized. If it is too large, the large errors at the side lobe region will prevent the algorithm from convergence. *Second*, each error term in Eq. (5) depends on all variables $\phi_{k,l}$ with orders as high as 4, making the derivative of Eq. (5) too complex and computationally prohibitive. As a result, these algorithms essentially need to search the solutions in randomized manner, which converges slowly and will very likely end up with a poor local optimum.

Differentiable pattern synthesis. To make the pattern synthesis converge to an optimal solution to phase shifts, we redesign an objective function, which is differentiable with a closed-form derivative. First, we *transform the problem into a new u-v coordinate* with $u = \frac{Nw_d \cos\phi\sin\theta}{\lambda}$, and $v = \frac{Nw_d \sin\phi\sin\theta}{\lambda}$. Accordingly, the reflection pattern F_{ϕ_r,θ_r} is transformed into:

$$F_{u,v} = \frac{1}{N}\sum_{k,l=-N/2}^{N/2-1} \sqrt{\sigma_0}e^{j\hat{\varphi}_{k,l}} \cdot e^{j\frac{2\pi}{N}(ku+lv)}, \tag{6}$$

where $\hat{\varphi}_{k,l} = \varphi_{k,l} + \frac{2\pi}{\lambda}\vec{p}_{k,l}^T\vec{e}_i$ is fixed, given that the BS and MilliMirror are static. Eq. (6) reveals that $F_{u,v}$ is the 2D Fourier transform of the phasors $e^{j\hat{\varphi}_{k,l}}$. According to Parseval's theorem, the total radiation power should satisfy:

$$\sum_{u,v=-N/2}^{N/2-1} |F_{u,v}|^2 = \sum_{k,l=-N/2}^{N/2-1} |\sqrt{\sigma_0}e^{j\hat{\varphi}_{k,l}}|^2 = N^2\sigma_0. \tag{7}$$

Given the total power $N^2\sigma_0$, the amplitude of the objective pattern $|\tilde{F}_{u,v}|$ can be clearly defined by distributing the total power equally to the u-v region that corresponds to the main lobe in the original polar coordinates.

Since $|\tilde{F}_{u,v}|$ does not contain the phase information and is not derivative with respect to $\hat{\phi}_{k,l}$, we optimize $\hat{\phi}_{k,l}$ based on the radiation power of the objective pattern $|\tilde{F}_{u,v}|^2$. Specifically, the pattern power $|F_{u,v}|^2$ can be represented as the 2N-point inverse Fourier transform of the 2D autocorrelation coefficients $R_{p,q}$ of the phase shifts [30]:
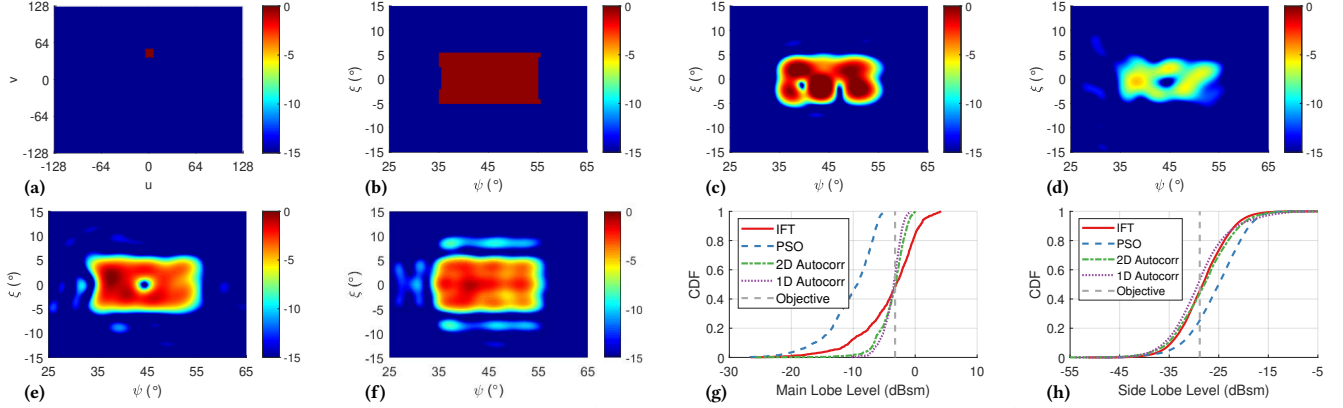
Figure 5: Comparison of the pattern synthesis methods. (a) Objective pattern in u-v coordinates. (b) Zoomed-in objective pattern in ψ-ξ coordinates. (c) Iterative Fourier transform. (d) Particle swarm optimization. (e) 2D autocorrelation. (f) 1D decomposition. (g) Distributions of MLL. (h) Distributions of SLL.

$$|F_{u,v}|^2 = \sum_{p,q=-N}^{N-1} R_{p,q} e^{\frac{2\pi}{2N}(p(2u)+q(2v))}, \text{ where}$$

$$R_{p,q} = \sum_{m,n=\max(-N/2,p-N/2)}^{\min(N/2-1,N/2-1-p)} \sigma_0 e^{j(\hat{\varphi}_{m+p,n+q}-\hat{\varphi}_{m,n})} \qquad (8)$$

Since $R_{p,q}$ uniquely determines $|F_{u,v}|^2$ via Fourier transform, the phase shifts $\hat{\varphi}_{k,l}$ can be optimized by minimizing the error E between the theoretical and objective $R_{p,q}$:

$$E = \sum_{p,q} |R_{p,q} - \tilde{R}_{p,q}|^2. \qquad (9)$$

Compared with Eq. (5), each error term in Eq. (9) is only related to a few phase shifts with an order of 2. A closed-form derivative can be calculated:

$$\frac{\partial E}{\partial \varphi_{k,l}} = \sigma_0 \text{Re}\Big\{ \sum_{p,q} \cos(R_{p,q} - \hat{R}_{p,q}) e^{j(\varphi_{k+p,l+q}-\varphi_{k,l}-\frac{\pi}{2})}$$
$$+ \sum_{p,q} \cos(R_{p,q} - \hat{R}_{p,q}) e^{j(\varphi_{k,l}-\varphi_{k-p,l-q}+\frac{\pi}{2})} \Big\}.$$

We then apply Newton's method [40] to solve Eq. (9) and obtain the phase weights $\varphi_{k,l}$, which are then used to determine the thickness of each unit element following Sec. 3.1.

Decomposing the 2D pattern synthesis to remove nulls. We compare our reflection beam synthesis method with the standard iterative Fourier transform [12] and particle swarm optimization [15], using an example MilliMirror surface with 64×64 MBDCs and $w_d = 1.25$ mm. To construct the MilliMirror model in HFSS, we use the solution of each algorithm when the objective errors converge or a maximum number of iterations (i.e., 1,000) is reached. In practice, the ϕ-θ coordinates has ambiguity around the $+Z$ axis, we instead use the ψ-ξ coordinates to define beams pointing out of the X-Y plane, i.e., the dielectric surface. As shown in Fig. 3b, we have $\psi = \text{atan}\frac{\cos\theta}{\sin\phi\sin\theta}$ and $\xi = \text{asin}(\cos\phi\sin\theta)$. Specifically, a beam pattern is defined as a quaternion $\vec{b} = (\psi_0, \xi_0, \Delta_\psi, \Delta_\xi)$, where ψ_0 and ξ_0 represents the direction of the beam center, Δ_ψ and Δ_ξ represents the beam width along the two perpendicular directions. As an example for comparison, we define a fan beam as $(45°, 0°, 20°, 10°)$.

Fig. 5a and b show the objective pattern in the u-v and ψ-ξ coordinates, respectively. Considering conservation of the power in Eq. (7), the objective pattern in Fig. 5a is the optimal pattern that can be achieved by MilliMirror. Fig. 5c, d, and e show the pattern generated by different methods. While all the methods create nulls within the main lobe region, the pattern synthesized by our method (Fig. 5e) is closest to the objective pattern (Fig. 5b) with the least number of nulls.

Unfortunately, nulls are inevitable when synthesizing 2D patterns, mainly due to two reasons. *First*, the MBDCs can only change the phase of the signal, limiting feasible space of the patterns generated by MilliMirror. *Second*, the 2D main lobe region and side lobe region depend on the same N^2 phase shifts and thus are coupled in a complex way. It is observed that minimizing the side lobe level results in nulls in the main lobe region, as shown in Fig. 5c, d, and e. For objective patterns with a single main beam, we propose to *find a suboptimal solution without nulls in the main beam by factorizing the 2D pattern synthesis into two 1D pattern synthesis*. Specifically, given an objective pattern $\tilde{F}_{u,v}$, we first find the maxima and minima of u and v of the main lobe. Then, we extend the main lobe to a rectangular region $\{(u,v)|u_{\min} \le u \le u_{\max}, v_{\min} \le v \le v_{\max}\}$. Since the transform of a regular beam in the u-v coordinates has a convex shape and can be approximated as a rectangle, as illustrated in Fig. 5a, the extension of the main beam only introduces a minor decrease of the MLL.

With a rectangular main lobe in the u-v coordinates, the 2D beam pattern can be factorized as the product of two 1D beam patterns, i.e., $F_{u,v} = F_u * F_v$, where

$$F_s = \frac{1}{\sqrt{N}} \sum_{k=-N/2}^{N/2} \sigma_0^{\frac{1}{4}} e^{j\hat{\varphi}_k} e^{j\frac{2\pi}{N}ks}, \text{ for } s = u, v \qquad (10)$$

Next, we apply the 1D version of the autocorrelation method to find the optimal phase shifts φ_k and φ_l for $\tilde{F}_u$ and $\tilde{F}_v$, respectively. Finally, the phase shift of each MBDC is determined as $\varphi_{k,l} = \varphi_k + \varphi_l$. Fig. 5f shows the pattern synthesized with the proposed decomposition method. A more flat main lobe without nulls is achieved thanks to the flat 1D patterns that are more easily synthesized.

Comparison of pattern synthesis algorithms. We quantize the quality of beam patterns synthesized by different algorithms
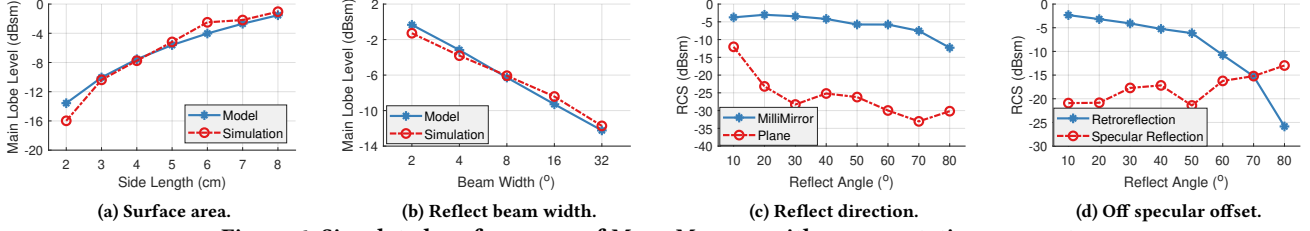
| (a) Surface area. | (b) Reflect beam width. | (c) Reflect direction. | (d) Off specular offset. |

Figure 6: Simulated performance of MILLIMIRROR with representative parameters.

Method	IFT	PSO	Autocorrelation	Decomposition
Time (s)	1.51	181.38	1220.81	1.82

Table 1: Covergence time of pattern synthesis algorithms.

using distributions of RCS in the main lobe and the side lobe. Fig. 5g shows the distributions of MLL. PSO fails to converge to the objective MLL. While the median MLL of IFT is close to the objective MLL, the main lobe has the highest variance. The autocorrelation method generates the optimal MLL. However, there are still nulls in the main lobe, as indicated by the long tail of the MLL distribution. In contrast, the decomposition method eliminates the nulls and achieves the lowest main lobe variance. Fig. 5e shows the distributions of SLL. Except for PSO that fails to converge, the other three methods achieve similar SLLs.

We further compare the convergence time of different algorithms. As shown in Tab. 1, the autocorrelation method has the longest convergence time due to the calculation of derivatives and update of phase shifts of all elements. In contrast, the decomposition method has a short convergence time comparable to the IFT method since it reduces the complexity of the optimization iteration from $O(N^2)$ to $O(N)$. It is much more efficient when N becomes large.

3.3 Microbenchmark Validation

We now conduct comprehensive experiments in HFSS to verify the correctness of our MILLIMIRROR design and characterize the performance of the pattern synthesis method.

Impact of surface area. We first evaluate how the size of MILLIMIRROR affects its RCS. According to the conservation of the power in Eq. (7), the ideal MLL of MILLIMIRROR is proportional to the area of MILLIMIRROR, assuming the incidence of a plane wave. We use HFSS to create MILLIMIRROR surfaces with an area from 2×2 cm^2 to 8×8 cm^2 and objective reflection beam as $(45°, 0°, 20°, 10°)$. Fig. 6a shows the increasing trend of MILLIMIRROR's MLL matches that of the theoretical objective MLL following Eq. (7). Thus, *when a link requires an extra gain G_e, it can be achieved by simply scaling up the area of MILLIMIRROR by G_e.*

Impact of beam width. We then evaluate the impact of beam width on the MLL by simulating MILLIMIRROR with different azimuth beam width from $2°$ to $32°$. Fig. 6b shows that the simulated MILLIMIRROR's MLL decreases by about 3 dB as the beam width is doubled. The decreasing trend matches that of the maximum MLL G_m of the objective beam pattern. That is, given a fixed total power, the MLL is halved as the main lobe region in the u-v coordinates doubles. The results indicates that *G_m can be used to accurately estimate the minimum size of MILLIMIRROR prior to running pattern synthesis*. We will elaborate on this in Sec. 6.

Impact of reflection direction. Similar to patch antennas, the

reflection field of view (FoV) of a MBDC must be narrower than half-space ($180°$). To benchmark the effective FoV of MILLIMIRROR with MBDCs, we create MILLIMIRROR with reflection pencil beams that deviate from the broadside direction by $10°$ to $80°$. As comparison, we simulate the reflection pattern of a plane with the same size and facing the broadside direction. While the RCS of the plane dramatically drops as the reflect angle deviates from the broadside direction, MILLIMIRROR consistently retain high RCS. Fig. 6c shows that the MLL of MILLIMIRROR only decreases by about 4 dB as the reflect angle increases to $70°$. Therefore, *the effective reflection FoV of the MBDC should be around $140°$ ($\pm70°$) at 4 dB tolerance.*

Impact of off-specular offset. MILLIMIRROR "violates" the Snell's law of reflection and resteers its reflect signal to off-specular directions. To evaluate MILLIMIRROR's re-steering capability, we consider an extreme case, *i.e.*, retroreflection, where the incident signal is reflected back to the source. *We create retroreflective MILLIMIRROR with incident angles deviating from the broadside direction by $10°$ to $80°$*. Fig. 6d compares the RCS at the main lobe and specular reflection directions. With the increase of the reflect angle, *the gain of retroreflection gradually drops while the specular reflection becomes stronger, mainly due to the limited FoV of the MBDC.* Given the 4 dB tolerance, the effective FoV of MILLIMIRROR should be around $100°$ ($\pm50°$).

4 WIDEBAND MILLIMIRROR

4.1 Beam Squint Effect

The basic MILLIMIRROR model in Sec. 3.2 assumes a single working frequency point f_0. Although the target beam can always be formed with a sufficiently large surface, the actual beam pattern is distorted when the frequency of the incident signal deviates from the carrier frequency f_0 by design. This phenomenon, known as the *beam squint* effect, imposes a constraint on the maximum size of the surface for a given bandwidth [37], whereas the size constraint in turn limits the maximum signal power that can be reflected.

The beam squint effect stems from the propagation delays of the signal incident at and reflected by different antennas. These propagation delays introduce phase delays that must be compensated by the antennas array with different phase shifts in order to generate the objective beam pattern. However, these phase delays vary inversely proportional to the signal wavelength, which cannot be fully compensated by the fixed phase shifts of the antennas. Such mismatch causes the distortion of the beam pattern generated by the antenna array. The beam squint effect imposes a constraint to the size of the reflectarray similar to traditional antenna arrays [23]:

$$Bd \leq \frac{c}{|\cos \gamma_i + \cos \gamma_r|},$$ (11)

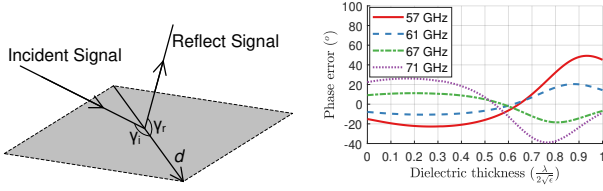where c is the light speed in free space. γ_i is the angle between the

Figure 7: Geometric relation for the beam squinting effect.
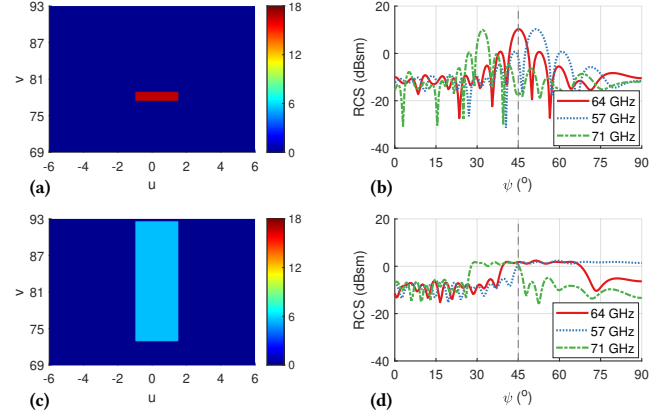
Figure 8: Phase errors of the MBDC.

Figure 9: Illustration of the wideband pattern synthesis. (a) Zoomed-in objective pattern for a single frequency. (b) Reflect pattern for a single frequency. (c) Zoomed-in objective pattern for a wide band. (d) Reflect pattern for a wide band.

incident signal and the maximum distance vector $\vec{d}$ connecting the two points on the MilliMirror surface (Fig. 7). γ_r is the angle between the reflected signal and $\vec{d}$. Intuitively, this constraint ensures that the pair of furthermost elements on a surface has a phase error smaller than 180° within the frequency band, i.e., $f_0 \pm \frac{B}{2}$, in order to avoid the destructive superimposition of the reflected signals.

Noted that *the beam squint problem disappears if the reflection beam points follows along the specular reflection direction of the surface*, i.e., when $\gamma_i + \gamma_r$ approaches 180° for all pairs of points on the surface. But in practice, the objective beam direction cannot always be aligned with the specular reflection direction, due to possible mounting orientation constraints of MilliMirror. Moreover, the specular reflection has very narrow beam width, which may not fulfil the objective patterns that require a wide beam.

To better understand the impact of beam squinting, we take the WiGig network [47] as an example. The latest WiGig standard specifies up to 14 GHz band (57-71 GHz), supporting multiple channels (2.16 GHz each). Suppose the incident direction $\phi_i = 90°$, $\theta_i = 0°$ and the reflection direction $\phi_r = 90°$, $\theta_i = 45°$, then $\gamma_i = 90°$ and $\gamma_r = 60°$. Following Eq. (11), the diagonal length d must be smaller than 27.8 cm for one WiGig channel, and only 4.3 cm for the entire 14 GHz band. Our empirical observation on HFSS shows that the RCS of a single MBDC with $w_d = 1.25$ mm is around -58.9 dBsm. So the maximum RCS achievable by MilliMirror with narrowest "pencil beams" is around 29.0 dBsm for a single channel, and becomes only -3.5 dBsm for the entire 14 GHz WiGig band!

We further simulate a beam pattern with the main lobe region as $(45°, 0°, 1°, 1°)$ for the MilliMirror with an area of 8×8 cm^2. Fig. 9a shows the objective pattern at center frequency $f_0 = 64$ GHz and Fig. 9b shows the corresponding azimuth pattern. While the desired pencil beam is generated at 64 GHz, it shifts away at edge frequencies of the working band and leaves nulls as low as -17 dBsm at the target reflection direction. This would significantly limit the actual advantages of MilliMirror.

4.2 Frequency Independent MilliMirror Model

We first identify the root cause of the beam squint effect in order to break the constraint in Eq. (11). According to Eq. (4), the reflection beam pattern of MilliMirror depends on three phase shifts, i.e., $\varphi_{k,l}$ caused by the MBDC, $\frac{2\pi}{\lambda} \vec{p}_{k,l}^T \vec{e}_i$ by the incident signal, and $\frac{2\pi}{\lambda} \vec{p}_{k,l}^T \vec{e}_r$ by the reflection signal. On the one hand, recall in Sec. 3.1, the thickness of the MBDC is limited within half of the effective wavelength. The change of $\varphi_{k,l}$ across different frequencies is thus minor. For example, Fig. 8 shows the phase errors of the MBDC at the WiGig band. By setting the center frequency $f_0 = 64$ GHz, most phase errors are smaller than 20° and the maximum error of 45° only occurs at the edge frequencies and a few thickness values. Thus,

it is feasible to approximate the phase shifts $\varphi_{k,l}$ as constants within the working band. On the other hand, the phase shifts $\frac{2\pi}{\lambda} \vec{p}_{k,l}^T \vec{e}_i$ and $\frac{2\pi}{\lambda} \vec{p}_{k,l}^T \vec{e}_r$ can dramatically change with frequency, since they are proportional to the size of MilliMirror.

It reveals an opportunity to *decouple the size and the bandwidth* of MilliMirror and synthesize frequency independent patterns. Let $\hat{u} = \frac{N w_d (\cos \phi_i \sin \theta_i + \cos \phi_r \sin \theta_r)}{\lambda}$ and $\hat{v} = \frac{N w_d (\sin \phi_i \sin \theta_i + \sin \phi_r \sin \theta_r)}{\lambda}$, the reflect pattern $F_{u,v}$ in Eq. 6 can be transformed into $F_{\hat{u},\hat{v}}$:

$$F_{\hat{u},\hat{v}} = \sum_{k,l=-N/2}^{N/2-1} e^{j\varphi_{k,l}} \cdot e^{j\frac{2\pi}{N}(k\hat{u}+l\hat{v})}. \tag{12}$$

Note that $F_{\hat{u},\hat{v}}$ is different from the $F_{u,v}$, in the sense that the optimization variables, i.e., $\varphi_{k,l}$, are independent from signal wavelength λ, which is embedded in the coordinates $\hat{u}$ and $\hat{v}$. Given the transformed objective, the decomposition method (Sec. 3.2) can be reused to find the frequency independent optimal phase shifts $\varphi_{k,l}$.

However, the main lobe regions of different frequencies is now transformed to different regions in the $\hat{u}$-$\hat{v}$ coordinates, since $\hat{u}$ and $\hat{v}$ are inversely proportional to the signal wavelength λ. To generate the objective main lobes at all frequencies, we *set the main lobe region in the objective pattern* $\tilde{F}_{\hat{u},\hat{v}}$ *as the union of the main lobe regions of all frequencies in the desired working band*. The pattern synthesized according to $\tilde{F}_{\hat{u},\hat{v}}$ will generate consistently strong reflection signals covering the objective main lobe region across the bandwidth. Notably, now that the power of the main beam is distributed over a wide region, the absolute MLL will be inevitably reduced compared with the single carrier case.

Fig. 9c shows the frequency independent objective pattern for the example in Sec. 4.1, and the corresponding azimuth pattern is shown in Fig. 9d. MilliMirror achieves a consistent RCS of 1 dBsm across the entire 57-71 GHz band. As $\tilde{F}_{\hat{u},\hat{v}}$ has a larger main lobe region, the RCS becomes weaker. Nonetheless, we can always increase the size of MilliMirror to compensate this loss, thanks to the key advantage of $\tilde{F}_{\hat{u},\hat{v}}$ in decoupling the size and the bandwidth. Specifically, according to the conservation of the energy in Eq. 7, by doubling the size of MilliMirror, the RCS increases by $10 log 10(2^2) = 6$ dB.
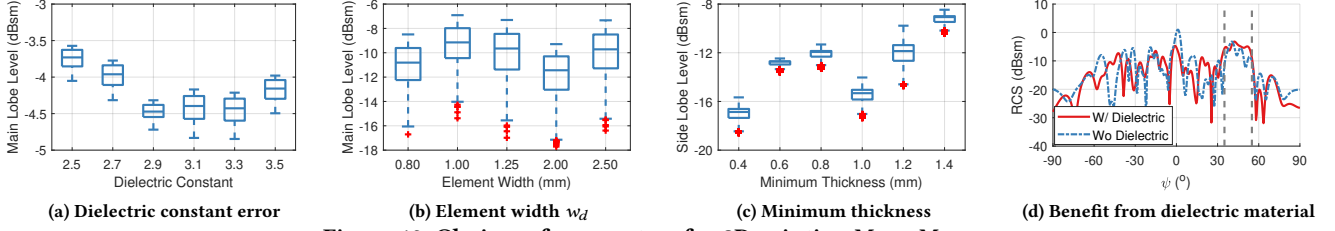
(a) Dielectric constant error **(b) Element width w_d** **(c) Minimum thickness** **(d) Benefit from dielectric material**

Figure 10: Choices of parameters for 3D printing MILLIMIRROR.

5 FABRICATION PROCESS

We use a standard 3D printing process to fabricate the dielectric part of MILLIMIRROR, which has a low cost but sufficiently high precision. Then, we coat a metal film on the back side of the 3D printed dielectric part. We now discuss the various design choices in the fabrication steps.

5.1 3D Printing Dielectric Surface

Selecting the dielectric material. According to Eq. (2), the surface impedance of the MBDC depends on the dielectric constant ϵ of the material. However, most off-the-shelf 3D printing materials only specify ϵ at very low frequencies, e.g., below 1 kHz. Nonetheless, it is known that ϵ decreases with frequency. Through a simple linear extrapolation of manufacture specified values, we speculate that the ϵ of most 3D printing material are around 2.5-3.5 at common RF frequencies. To evaluate the impact of an inaccurate ϵ, we synthesize a pencil beam pattern for the 4×4 cm^2 MILLIMIR-ROR assuming $\epsilon = 2.5$, and use HFSS to simulate its pattern with $\epsilon \in [2.5, 3.5]$. Fig. 10a shows that the MLL of the beam decreases slightly as the error of ϵ increases. This indicates MILLIMIRROR can be reliably fabricated even with an approximate ϵ.

In practice, we fabricate samples with some common printing materials, e.g., HP PA 12 [24], VisiJet M3 [53], and StratasSys Ve-roClear [52]. The samples made from HP PA 12 have the highest elongation at break and the lowest extension of warping, which is the most suitable for the follow-on metal deposition steps. Thus, we select HP PA 12 for the rest of MILLIMIRROR samples. The thicknesses of MBDCs are quantized with a resolution of 0.1 mm. Fig. 11a showcases the zoomed-in MBDCs of one such sample. By visually checking the samples, we observe that the relative thicknesses of MBDCs follow those in the models. It means that the maximum thickness error is no more than 0.1 mm, translating to a maximum phase error of about 14.5^o. Moreover, all MBDCs tend to have similar fabrication errors and experience similar phase shifts, which do not distort the beam pattern significantly. To minimize the impact of the ϵ error, we further request professional measurement service from KEYCOM [29], and measure ϵ as follows: First, a square HP PA 12 sample with 1 mm thickness is placed between the Tx and Rx, which consist of a horn antenna and a lens to shape the signals into plane waves. Then, the Tx scans a frequency band of 50-67 GHz and the ϵ at each frequency is deduced from the signal attenuation measured at the Rx and averaged to output the final report. The measurement confirms $\epsilon = 2.55$ around the 60 GHz band.

Element width. The width w_d of the MBDC is another crucial parameter to be determined before fabrication. To evaluate its impact, we run simulation for a 4×4 cm^2 MILLIMIRROR with w_d ranging from 0.8 mm to 2.5 mm. The objective pattern has a

fan beam $(45°, 0°, 10°, 10°)$. Fig. 10b shows that different element widths only have minor impact on the MLL. Nonetheless, we select $w_d = 1.25$ mm for two reasons. On one hand, w_d should be as large as possible to reduce the impact of the quantization errors of 3D printing and to make the back side of MILLIMIRROR less rugged and easier to coat metal. On the other hand, w_d must be smaller than $\frac{\lambda}{4}$ to avoid aliasing of the Fourier transform in Eq. (12). Specifically, according to the definition of Fourier transform, the indices $\hat{u}$ and $\hat{v}$ must be within $[-\frac{N}{2}, \frac{N}{2})$. Since both the coefficients $\cos \phi_i \sin \theta_i + \cos \phi_r \sin \theta_r$ and $\sin \phi_i \sin \theta_i + \sin \phi_r \sin \theta_r$ have a maximum value of 2, the element width w_d must be smaller than $\frac{\lambda}{4}$. For the WiGig frequency band, the w_d is thus around 1.25 mm.

Minimum thickness. To ensure structure strength, 3D printing usually has a requirement of the minimum thickness of the sample, denoted as δ_t. For example, HP PA 12 requires a minimum thickness of 0.4 mm. For MILLIMIRROR, this can be achieved by *shifting the range of the dielectric cuboid thickness by a δ_t constant* to $[\delta_t, \delta_t + \frac{\lambda}{2\sqrt{\epsilon}}]$. To evaluate the impact of δ_t, we simulate MILLIMIRROR with $\delta_t \in [0.4, 1.4]$ mm. Fig. 10c shows that *the SLL at the specular reflection direction dramatically increases with thicker dielectric cuboids*. The main reason is that a thicker dielectric entails the signal to travel a longer distance within MILLIMIRROR, which magnifies the mismatch between the theoretical and simulated models of MILLIMIRROR. Such mismatch distorts the pattern by creating a strong side lobe towards the specular reflection direction [33]. Thus, we set the minimum thickness to be 0.4 mm.

Necessity of the dielectric layer. An alternative element design is to remove the dielectric cuboid of the MBDC and assume a virtual vacuum cuboid with $\epsilon = 1$. All elements can be connected via a common metal base as in [58] and each element is simply a vaccum groove (VG). We simulate MILLIMIRROR with the two types of elements where $\psi_i = 0°$, $\xi_i = 0°$, and the objective pattern is a fan beam $(45°, 0°, 20°, 10°)$. Fig. 10d shows the azimuth patterns of the two structures. The SLL of the VG at the specular reflection direction is even large than the MLL, indicating significant mismatch between its theoretical and simulated models. The mismatch likely stems from the larger depth of the VG compared with the thickness of the MBDC, which introduces larger phase errors and thus stronger specular reflection. In addition, when the dielectric cuboid is used, the illumination area of all elements is increased thanks to the refraction effect of the dielectric material, and the mismatch is thus reduced. This further signifies the need of using MBDC as the unit element in MILLIMIRROR.

5.2 Depositing Metal Film

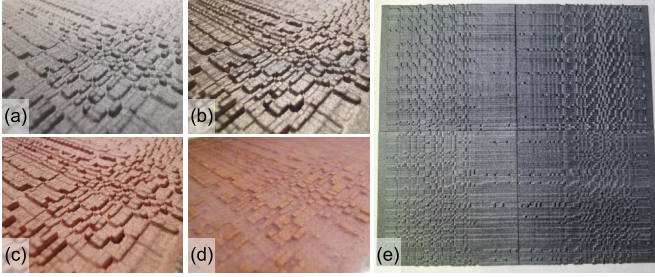MILLIMIRROR's metal film should block the transmission of the

Figure 11: Illustration of the fabrication process of MilliMirror. (a) After 3D printing. (b) After sputtering. (c) After electroplating. (d) After sealing with EcoFlex. (e) Scaling up MilliMirror with small modules.

incident signal and maximize the reflection. Thus, the thickness of the metal film should be at least several times of the skin depth (defined as the depth up to which the magnetic field penetrates inside the material) of the metal [61]. For example, the skin depths of copper at 60 GHz and 1 GHz are about 266.2 nm and 2.06 μm, according to the approximate model $\frac{1}{\pi f \mu \sigma}$ [55], where σ and μ are the conductivity and permeability of the metal, respectively. Further considering the erosion and oxidization of the metal, we set the thickness of the metal film as 15 μm.

The coating process consists of two steps. First, sputtering is applied to coat a thin layer of metal at the back of the 3D printing part and make the surface conductive [48]. Specifically, we sputter a 10 nm Cr layer to increase bonding strength between the metal layer and the dielectric layer and then a 300 nm copper layer is sputtered on top as the conductive layer for further electroplating process. Fig. 11b shows the sample after sputtering.

Then, we conduct the electroplating process [41] to increase the metal thickness at a faster deposition rate. We prepare electrochemical bath solution containing 74.88 g CuSO$_4 \cdot$5H$_2$O, 67.524 mL 98wt.% H$_2$SO$_4$, 1173 mL deionized water, 0.327 g NaCl, and 1.876 g Polyethylene Glycol (Mw=3350). This compost solution can be used to deposit metal on 8 samples of 10×10 cm^2 and scaled for MilliMirror with different sizes. Then, the sputtered dielectric surface and a copper plate are put into the solution, separated 8 cm apart, and face right towards each other. The surface current is generated by a Keithley 2400 electrometer, with current density set to 7 mA/cm^2 for 60 min to generate a 15 μm copper layer. The thickness is tunable with deposition time and current density. The sample after electroplating is shown in Fig. 11c. Finally, we seal the metal film with an encapsulation polymer (EcoFlex) to mitigate the oxidization of copper, as shown in Fig. 11d.

With this fabrication process, the total cost of a 10×10 cm^2 MilliMirror sample is about $15.3. The size can be customized and the cost scales accordingly. In contrast, PCB fabrication can only use bulk substrates with fixed sizes, $e.g.$, $9'' \times 12''$ Rogers 4350B and CLTE-MW. The amortized cost of a single layer 10×10 cm^2 patch antenna array at mmWave frequency is about $200. The size of a single MilliMirror sample can be limited by the volumes of the fabrication devices, e.g., the 3D printer, the sputter coater, and the beaker for electroplating. Fortunately, it is straightforward to scale up MilliMirror by fabricating small modules and splicing them together, as shown in Fig. 11e.

6 DEPLOYMENT OF MILLIMIRROR

Although natural reflectors such as building walls can create NLoS paths, they are highly opportunistic and impacted by the reflector orientation and material. For example, smooth concrete reflects signals strongly but only specularly, whereas textured concrete/brick results in significant scattering and attenuation [32]. MilliMirror can serve as an artificial reflector to overcome these limitations.

The deployment of MilliMirror can follow the standard practice of cellular network planning [49]. With simulation or field measurement, the blind spots of a BS can be identified. To cover each blind spot, we further identify candidate mounting positions of the MilliMirror by searching for suitable mounting structures around, $e.g.$, walls and traffic posts. Then, with the location of the BS, the location and orientation of the MilliMirror, and the blind spot region, the objective beam pattern of the MilliMirror can be determined by projecting the blind spot region to the unit sphere centering at the MilliMirror. Finally, the pattern synthesis algorithm in Sec. 3.2 is applied to find the MBDC thicknesses.

We note that *the minimum size of MilliMirror can be estimated prior to the pattern synthesis process, given the link budget and MilliMirror mounting position.* Suppose MilliMirror consists of $N \times N$ MDBCs whose reflect gain is σ_0, the main lobe region of the objective beam pattern occupies A out of N^2 points in the entire u-v space. The objective MLL G_m can be obtained by evenly distributing the power across the A points, $i.e.$, $G_m = \frac{N^2 \sigma_0}{A}$. Along the deterministic Tx-MilliMirror-Rx path, the minimum Rx power follows the Friis law: $P_r = \frac{P_t G_t G_r \lambda^2 G_m}{(4\pi)^3 d_t^2 d_r^2}$, where P_t, G_t, G_r are the Tx power, Tx gain, and Rx gain, which are known based on the Tx/Rx specs. d_t (d_r) is the distance between the Tx (Rx) and MilliMirror. Since all these parameters are available when the mounting location and orientation of MilliMirror is known, we can estimate the required size of MilliMirror as: $N = \sqrt{\frac{(4\pi)^3 d_t^2 d_r^2 A}{P_t G_t G_r \lambda^2 \sigma_0}}$.

MilliMirror is fully passive and can operate transparently to the standard mmWave radios. The standard beam searching process, such as in 802.11ad and 5G NR, all require that the BS/client periodically scan a set of beams, and the beam with highest RSS is picked to establish the link. With MilliMirror, the BS/client will automatically find it optimal to point towards the MilliMirror surface, as it establishes the only or the best NLoS path between them. We will verify this salient property of MilliMirror below.

7 EVALUATION

7.1 Experimental Setup

We fabricate MilliMirror following the process in Sec. 5 and conduct field tests using off-the-shelf 802.11ad devices from Airfide [3], as shown in Fig. 12a. An Airfide radio arranges 8 6×6 uniform planar arrays into a large planar array. The beam patterns of the array can be controlled by the beamforming weights defined in a codebook. The weight for each antenna element comprises a 2-bit phase shift ($i.e.$, 0, 90$°$, 180$°$, and 270$°$) and a 1-bit amplitude ($i.e.$, on and off). At the Tx side, we activate all 8 arrays and generate a pencil beam pointing towards MilliMirror. To determine the beamforming weights, we calculate the theoretical steering vector for antennas, compensate for the constant initial phases of the antennas [66], and approximate the weights with the closest
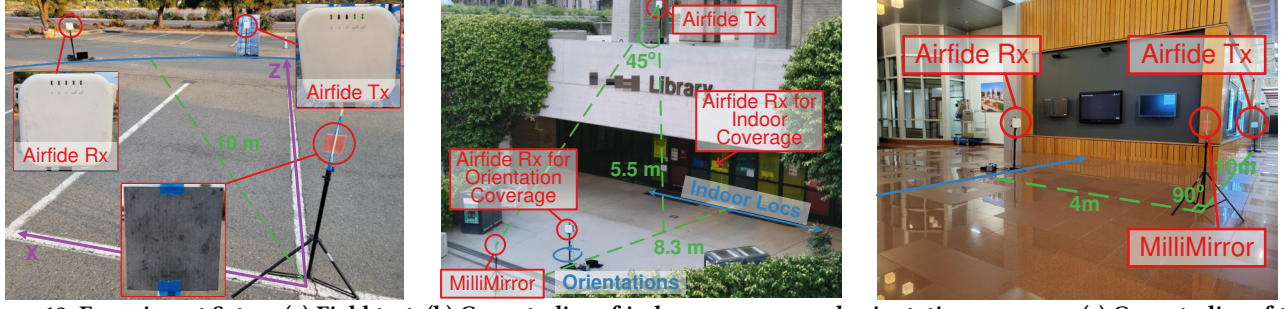
Figure 12: Experiment Setup. (a) Field test. (b) Case studies of indoor coverage and orientation coverage. (c) Case studies of the around the corner scenario.

RSS (dBm)	-68	-66	-65	-64	-63
Data rate (Mbps)	385	770	962.5	1155	1540
RSS (dBm)	-62	-61	-59	-55	-54
Data rate (Mbps)	1925	2310	2502.5	3080	3850

Table 2: Mapping between RSS and data rate.

quanitzed phase shifts. The azimuth and elevation beamwidth of the pencil beam with highest directionality is about $4.8°$ and $9.5°$, respectively. At the Rx side, we can only activate one antenna element due to the configuration limitation of the device in the Rx mode. The Rx reports the RSSI of the received beacons, which have linear relationship with RSS (in dBm) output by the "iw scan" command, i.e., $RSS \propto 0.0652RSSI - 74.3875$. Thus, we use RSS as the metric to evaluate the gain from MilliMirror. Note that RSS can be monotonically mapped to the link data rate and -68 dBm is the minimum to establish a link [7]. Tab. 2 shows the MCS indices and corresponding data rates supported by the Airfide radio.

7.2 Field Test

We conduct field tests to evaluate the beamforming patterns and scalability of MilliMirror. The experiments run in an open parking lot with movable NLoS obstacles, as shown in Fig. 12a. The Tx is surrounded by a cardboard covered with foil paper, which blocks the direct LoS path to the Rx. Both the Tx and Rx are 10 m away from the MilliMirror, so the NLoS path via MilliMirror is 20 m in total. The Rx is moved along the 10 m semicircle centered at MilliMirror. A laptop is connected to the Rx to log the RSSI. The local coordinates of MilliMirror is defined as in Fig. 12, where the x-axis is parallel to the surface and to the left side, and the z-axis is to the front normal direction.

Accuracy of beam pattern synthesis. We fabricate MilliMirror samples with representative reflection beam patterns, including single pencil beam, multi-armed pencil beams, and single fan beam. These samples have area of $10 \times 10 \ cm^2$ (6,400 MBDCs). Note that angular range within $10°$ of the direction of the Tx is not measured, since it is hard to place both the Tx and Rx in the small spot. In practice, it is unlikely that an Rx falling in this angular range is fully blocked from the Tx.

We measure the reflection beam patterns of two MilliMirror samples with single pencil beam towards $\psi = 45°$ and $-45°$, and one sample with two-arm pencil beams towards $\psi = 25°$ and $\psi = 45°$. As shown in Fig. 13, the samples indeed create high-directionality pencil beams towards the desired directions. Theoretically, the MLL with two-arm pencil beams should be 3 dB weaker than that with

single pencil beam due to equal power splitting. However, the measured difference in MLL is about 5 dB. This is due to the *inevitable side lobes when synthesizing multi-armed beams using phase-only unit reflection elements*. Specifically, the ideal beamforming weights of a multi-armed beam are the sum of the steering vectors to all beamforming directions and thus have different amplitudes. They cannot be accurately achieved by the phase-only weights of MilliMirror and this mismatch causes unwanted side lobes. Thus, given multiple target directions, it is better to deploy multiple isolated MilliMirror surfaces reflecting towards each direction, in order to avoid the power wastage on side lobes.

We further measure the two samples each a single fan beam, i.e., $(45°, 0°, 10°, 5°)$ and $(45°, 0°, 20°, 5°)$. As shown in Fig. 14, *the beamwidths of the measured beam patterns match the design well*. As the main beam region doubles from $10°$ to $20°$, the MLL decreases by 3.5 dB on average, approximating the theoretical 3 dB difference.

Scaling up the MilliMirror surface. We further show how MilliMirror's reflection gain inceases as its physical dimension scales up. Specifically, we fabricate 3 MilliMirror samples with size of $8 \times 8 \ cm^2$ (4,096 MBDCs), $16 \times 8 \ cm^2$ (8,192 MBDCs), and $16 \times 16 \ cm^2$ (16,384 MBDCs). All samples are designed to create a fan beam $(45°, 0°, 10°, 5°)$. Fig. 15 shows the angular reflection gain pattern between $35°$ and $55°$. We observe that all 3 samples generate the expected beamwidth of around $10°$. *The MLL steps up by around 3 dB as the surface area doubles, which matches our model in Sec. 3*. As the line-of-sight path between the Tx and the Rx is blocked, the RSS due to surrounding natural reflectors is only around -68 dBm, where the data link is hardly established. Using $8 \times 8 \ cm^2$, $16 \times 8 \ cm^2$, and $16 \times 16 \ cm^2$ MilliMirror samples improves the RSS by 7, 10, and 14 dB respectively, which approximately translates into the bit rates of 2310, 2502.5, and 3850 Mbps according to the specification of WiGig [7]. The RSS fluctuation within the main lobe may be due to slight tilting and warping of the samples, which is loosely attached to the tripod. These minor errors can be avoided in practice by designing more sturdy mechanical mounting structures.

Scaling across a wideband. To evaluate the scalibility of MilliMirror across a wideband, we fabricate two MilliMirror samples with the narrowband model (Sec. 3) and the wideband model (Sec. 4). The narrowband sample generates a pencil beam towards $45°$ at 60.48 GHz. In contrast, the wideband sample is designed to work on all the 3 802.11ad channels supported by the Airfide radio (centered at 58.32, 60.48 and 62.64 GHz). The result in Fig. 16 shows that the narrowband sample experiences a significant beam squint
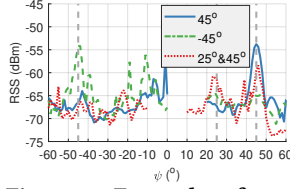
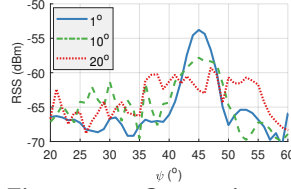**Figure 13: Examples of pencil beam patterns**
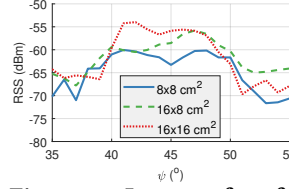

Figure 14: Comparison of main beam width
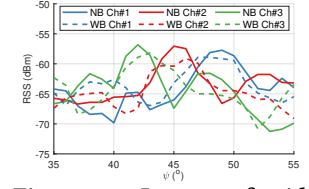

Figure 15: Impact of surface area
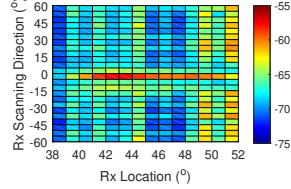

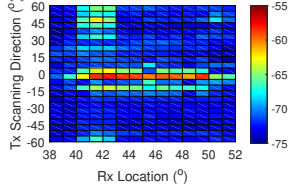**Figure 16: Impact of wideband**

Figure 17: Tx beam selection

Figure 18: Rx beam selection

effect. While it creates a pencil beam towards $45°$ at 60.48 GHz, the beam shifts to around $49°$ at 58.32 GHz and $42°$ at 62.64 GHz, leading to a loss of about 11 dB at the desired direction! The MLL of the narrowband sample at the three channels is -67 dBm (385 Mbps), -57 (2502.5 Mbps), and -66 dBm (770 Mbps), respectively. In contrast, despite the beam squint effect, the wideband sample still retains high reflection gain across different channels, at the cost of MLL degradation compared with the best MLL of the narrowband sample. Specifically, its MLL at the three channels is -61 dBm (2310 Mbps), -60 (2310 Mbps), and -63 dBm (1540 Mbps), respectively. The result verifies the effectiveness of MilliMirror's wideband model.

Transparent operation of MilliMirror in mmWave networks. MilliMirror is fully passive and does not require coordination with existing network devices. To showcase such transparency, we reuse the sample with a fan beam $(45°, 0°, 10°, 5°)$. The Tx runs a standard linear beam searching protocol, where it scans within the $−60°$ to $60°$ azimuth plane at a step of $5°$. The MilliMirror surface is located at the normal direction of the Tx. Meanwhile, we move the Rx around the fan beam region of MilliMirror. Fig. 17 shows the RSS of all the Tx beams measured by the Rx. As long as the Rx is within the designed fan beam region of MilliMirror, the $0°$ Tx beam always leads to the strongest RSS and will be selected as the best by the beam searching protocol. Thus, *the Tx always settles on the direction of MilliMirror even without knowing its existence.*

MilliMirror follows the the principle of channel reciprocity and provides the same gain to both the downlink and the uplink. To verify this, we reverse the above experiment, allowing the Rx to scan from $−60°$ to $60°$ and record the RSS measured at the Tx. As shown in Fig. 18, when the Rx is within the fan beam region of MilliMirror, the strongest RSS is achieved with the beam pointing towards MilliMirror, which always resteers the signal back to the Tx.

7.3 Case Study

We now demonstrate several representative use cases of MilliMirror for both mmWave coverage expansion.

Outdoor-to-indoor coverage. We first show how MilliMirror enables outdoor-to-indoor links around a two-floor building, as shown in Fig. 12b. The Tx is placed at the 2nd floor 5.5 m above the ground, with its phased arrays pointing away from the building. A 10×10 cm^2 MilliMirror sample (6,400 MBDCs) is placed at

the 1st floor, has an elevation angle of $45°$ relative to the Tx, and faces towards the building windows at the 1st floor. It receives signals incident at $\psi = 0°$, $\xi = −45°$ and generates a reflect fan beam $(0°, 0°, 20°, 2°)$. The Rx is 8.3 m away from the sample and besides the window at the 1st floor. It is moved tangentially within a distance of 6 m relative to the sample (the blue line segment near the window in Fig. 12b). The center of the Rx trace is at the direction of the center of MilliMirror's fan beam, i.e., $\psi = 0°$, $\xi = 0°$.

Fig. 19 shows that, the RSS without the sample is only around -71 dBm, which can only establish the 802.11ad control channel with bit-rate 23 Mbps. The MilliMirror sample can illuminate a tangential range of about 3 m and amplifies the RSS to -66 dBm on average, which translates to a data rate of 770 Mbps. Note that the RX is 8.3 m away from MilliMirror and the azimuth beamwidth of the MilliMirror sample is $20°$. This translates to a theoretical tangential coverage of about 2.9 m, which matches the experimental coverage. In practice, multiple MilliMirror samples can be co-located to cover a wider FoV, and a larger MilliMirror can penetrate more deeply into the building.

Overcoming orientation sensitivity. mmWave signals are easily blocked by human bodies and the link quality depends on the orientation of the user [59]. We now demonstrate how MilliMirror can make the mmWave links less sensitive to user orientation. The experiment is conducted at the same two-floor building as above, except that the Rx is placed at a different location, separated from MilliMirror by 2.3 m, as shown in Fig. 12b. Since the Rx antenna FoV is less than $120°$, we rotate it to emulate different user orientations (the blue circle). Fig. 20 shows that, when the Rx faces towards the Tx (*i.e.*, $180° − 360°$), the RSS is similar with and without MilliMirror. In contrast, when the Rx faces away from the Tx (*i.e.*, $0° − 180°$), MilliMirror improves the RSS by about 10 dB. In practice, full $360°$ coverage can be enabled by deploying multiple MilliMirror samples as a low-cost way to improve the robustness of the mmWave links.

Around the corner coverage. By placing MilliMirror at a corridor intersection, the blind spot around the corner can be illuminated. We conduct an experiment in an indoor lobby, as shown in Fig. 12c. The MilliMirror is placed at the corner, receiving signals from $\psi = −45°$, $\xi = 0°$, and reflecting a fan beam $(45°, 0°, 20°, 2°)$. The Tx is 10 m away from MilliMirror; whereas Rx is 5 m away moved across 6 m distance (the blue line segment). Fig. 21 compares the RSS with MilliMirror, a copper plane reflector with the same size as MilliMirror, and the tripod without reflectors. While the copper plane creates a stronger main lobe towards the specular direction, the RSS drastically drops as the Rx is moved to anomalous directions, For example, the RSS drops to -62 dBm (1925 Mbps) when the Rx is moved by 1.6 m. In contrast, MilliMirror reshapes the incidental beam to cover a wider angular range and thus a larger
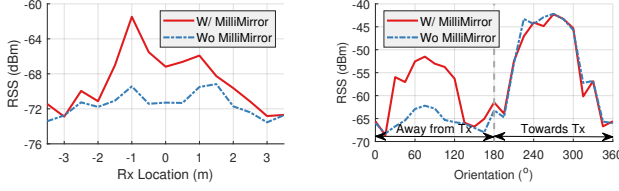
Figure 19: Outdoor to indoor coverage

Figure 20: Coverage of user orientations

Figure 21: Around the corner coverage

Figure 22: Performance in diverse scenarios

region around the corner. When the Rx moves by 1.6 m, the RSS still remains as high as -58 dBm (2502.5 Mbps).

8 DISCUSSION AND FUTURE WORK

Channel dynamics and multipath. To better understand the performance of MILLIMIRROR in different channel conditions, we measure the RSS improvement with MILLIMIRROR in some representative scenarios, including parking lot, roadside, lawn, and indoor lobby. We reuse the samples creating pencil beams. Due to the deployment limitation, we mount the Airfide radios and MILLIMIRROR on tripods and place them at the same height up the ground. Both distances of the Tx and Rx from MILLIMIRROR are 10 m. The LoS between the Tx and the Rx is blocked via a metal obstacle. Fig. 22 shows the RSS with and without MILLIMIRROR in different scenarios. The link achieves the highest gain in the parking lot and lawn, where few objects create strong NLoS signals. The gain in roadside is lower mainly due to the uneven ground of the road. In practice, accurate measurement must be conducted to reduce the relative location and orientation error of MILLIMIRROR. In contrast, thanks to the rich multipath, the RSS in indoor scenarios is higher than in outdoor scenarios. Nonetheless, MILLIMIRROR can still improve RSS by covering occasional blind spots, such as around the corner cases.

The channel between a MILLIMIRROR and a blind spot may have multipath and temporal dynamics. Simply synthesizing the beam that geometrically covers the blind spot may not be optimal due to multipath fading and occasional blockage of objects passing by. One solution is to deploy multiple MILLIMIRROR surfaces at different locations covering one blind spot and let the base station select the strongest beam (likely reflected by the best surface) at runtime. We leave such solutions for our future exploration.

Limitation of metallic reflecting surfaces. Metallic reflectors have been explored to extend cellular coverage [31, 42]. We simulate the RCS of cylindrical metallic surfaces with different sizes and curvatures as a preliminary inspection. The curvature is normalized, with 0 representing a flat surface and 1 a half-cylindrical surface. Fig. 23a shows that a larger curvature leads to a larger main lobe width, whereas Fig. 23b shows that a larger surface size reduces the main lobe width and increases the main lobe level. It is thus feasible to generate a reflection beam with specific width and level by jointly tuning the curvature and size of the surface. However, the simple cylindrical surfaces may create large ripples in the main lobes due to the destructive reflections from different surface parts. Designing metallic reflecting surfaces with arbitrary beam patterns may entail fabricating fine metal structures with similar granularity as MILLIMIRROR, which is challenging in practice. To our knowledge, this problem has not been addressed by any prior
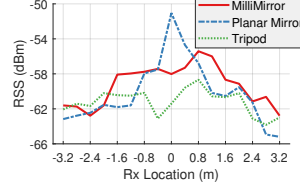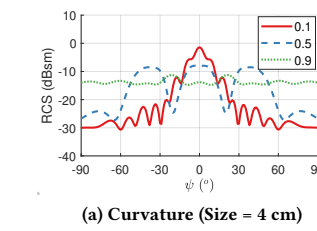

(a) Curvature (Size = 4 cm)

(b) Size (Curvature = 0.1)
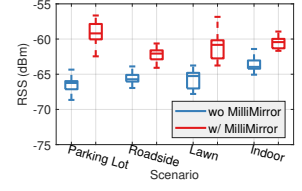
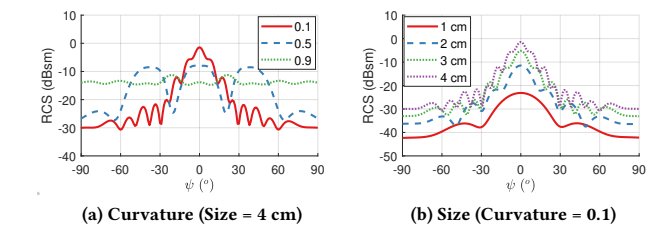**Figure 23: RCS of cylindrical metallic surfaces.**

work and could be a direction for future exploration.

Reconfigurable metasurface. MILLIMIRROR is mainly used to cover blind spots of wireless networks. A blind spot may appear due to the change of the infrastructure or the environment, *e.g.*, the construction of a new building. In such a case, it is easy to design and deploy a new MILLIMIRROR, thanks to its low cost, rapid fabrication, and easy installation. Typically, a MILLIMIRROR serves a fixed base station to cover one of its blind regions. The base station can thus communicate with a mobile user by blind beamforming to the MILLIMIRROR that covers the corresponding blind region. In contrast, an active metasurface with reconfigurability may also cover the blind spot by searching for a new beam pattern. However, given the stringent symbol-level beam switching of millimeter-wave communication and inaccessibility of signaling information at metasurfaces, the coordination between an active metasurface and the transceivers is still an open problem, and may need a separate control channel. Our correspondence with 5G carriers and infrastructure builders also indicates that fully passive reflecting surfaces are the most promising solution to solve the coverage problem of millimeter-wave communication.

9 CONCLUSION

We have designed, fabricated, and validated MILLIMIRROR, a 3D printed reflecting metasurface to expand mmWave coverage. Our design is driven by a closed form model that enables efficient and accurate reflection beam synthesis across a wide band. Our model can be easily generalized to accommodate different frequencies, beam patterns, and surface sizes. Beyond transparent integration into standard mmWave networks, we envision that MILLIMIRROR can be adapted to expand the sensing coverage of mmWave radars. We confirm this work does not raise any ethical issues.

ACKNOWLEDGMENTS

REFERENCES

[1] Omid Abari, Dinesh Bharadia, Austin Duffield, and Dina Katabi. 2017. Enabling High-Quality Untethered Virtual Reality. In *In Proceedings of USENIX NSDI*.

[2] Federico Agnoletto, Pau Castells, Emanuel Kolta, and Dennisa Nichiforov-Chuang. 2020. The economics of mmWave 5G: An assessment of total cost of ownership in the period to 2025. *GSMA Intelligence* (2020).

[3] Airfide. 2021. Airfide, a 5G Sorfware Company. https://airfidenet.com/.

[4] Abdulrahman Ahmed Ghaleb Amer, Syarfa Zahirah Sapuan, Nasimuddin Nasimuddin, Arokiaswami Alphones, and Nabiah Binti Zinal. 2020. A comprehensive review of metasurface structures suitable for RF energy harvesting. *IEEE Access* 8 (2020), 76433–76452.

[5] Venkat Arun and Hari Balakrishnan. 2020. RFocus: Beamforming using thousands of passive antennas. In *In Proceedings of USENIX NSDI*.

[6] VS Asadchy, Ana Díaz-Rubio, SN Tcvetkova, D-H Kwon, Amr Elsakka, Mohamed Albooyeh, and SA Tretyakov. 2017. Flat engineered multichannel reflectors. *APS Physical Review X* 7, 3 (2017), 031046.

[7] IEEE Standards Association. 2012. IEEE Standards 802.11ad-2012: Enhancements for Very High Throughput in the 60 GHz Band.

[8] D Berry, R Malech, and W Kennedy. 1963. The reflectarray antenna. *IEEE Transactions on Antennas and Propagation* 11, 6 (1963), 645–651.

[9] Michael Boyarsky, Timothy Sleasman, Mohammadreza F Imani, Jonah N Gollub, and David R Smith. 2021. Electronically steered metasurface antenna. *Nature Scientific reports* 11, 1 (2021), 1–10.

[10] Bao-Jie Chen, Huan Yi, Kung Bo Ng, Shi-Wei Qu, and Chi Hou Chan. 2016. 3D printed reflectarray antenna at 60 GHz. In *In Proceedings of IEEE ISAP*.

[11] Lili Chen, Wenjun Hu, Kyle Jamieson, Xiaojiang Chen, Dingyi Fang, and Jeremy Gummeson. 2021. Pushing the physical limits of iot devices with programmable metasurfaces. In *In Proceedings of USENIX NSDI*.

[12] Youji Cong, Guonian Wang, and Zhengdong Qi. 2015. A pattern synthesis method for large planar antenna array. *Progress in Electromagnetics Research M* 43 (2015), 147–156.

[13] CJ Davenport and JM Rigelsford. 2014. Slanted-comb frequency selective surface for use in reducing specular scatter for TM polarization. In *Proceedings of IEEE LAPC*.

[14] Paul I Deffenbaugh, Thomas M Weller, and Kenneth H Church. 2015. Fabrication and microwave characterization of 3-D printed transmission lines. *IEEE Microwave and wireless components letters* 25, 12 (2015), 823–825.

[15] Sanjay Kumar Dubey and Debasis Mandal. 2021. Digitally Controlled Steered Dual Beam Pattern Synthesis of a Rectangular Planar Array Antenna in a Range of Azimuth Plane Using Evolutionary Algorithms. *EMW Progress In Electromagnetics Research C* 114 (2021), 185–202.

[16] Manideep Dunna, Chi Zhang, Daniel Sievenpiper, and Dinesh Bharadia. 2020. ScatterMIMO: Enabling virtual MIMO with smart surfaces. In *In Proceedings of ACM MobiCom*.

[17] Mario D'Auria, William J Otter, Jonathan Hazell, Brendan TW Gillatt, Callum Long-Collins, Nick M Ridler, and Stepan Lucyszyn. 2015. 3-D printed metal-pipe rectangular waveguides. *IEEE Transactions on Components, Packaging and Manufacturing Technology* 5, 9 (2015), 1339–1349.

[18] Caroline Gabriel. 2020. Verizon lines up three partners to address the mmWave 5G coverage challenge. https://rethinkresearch.biz/articles/verizon-lines-three-partners-address-mmwave-5g-coverage-challenge/.

[19] Dongxing Gao, Rui Yang, Dong Li, Jiacheng Li, Zhenya Lei, and Fushun Zhang. 2018. Meta-surface based convex reflectors for generating highly directive pencil-beams and fan-beams. *OSA Optical Materials Express* 8, 5 (2018), 1359–1367.

[20] Marco Giordani, Michele Polese, Arnab Roy, Douglas Castor, and Michele Zorzi. 2018. A tutorial on beam management for 3GPP NR at mmWave frequencies. *IEEE Communications Surveys & Tutorials* 21, 1 (2018), 173–196.

[21] Thomas H Hand, Jonah Gollub, Soji Sajuyigbe, David R Smith, and Steven A Cummer. 2008. Characterization of complementary electric field coupled resonant surfaces. *AIP Applied Physics Letters* 93, 21 (2008), 212504.

[22] Saif Hannan, Mohammad Tariqul Islam, Ali F Almutairi, and Mohammad Rashed Iqbal Faruque. 2020. Wide bandwidth angle-and polarization-insensitive symmetric metamaterial absorber for X and Ku band applications. *Nature Scientific Reports* 10, 1 (2020), 1–9.

[23] Randy L Haupt. 2010. *Antenna arrays: a computational approach.* John Wiley & Sons.

[24] HP. 2021. HP 3D High Reusability PA 12. https://www.materialise.com/en/manufacturing/materials/pa-12-mjf.

[25] Chongwen Huang, Sha Hu, George C Alexandropoulos, Alessio Zappone, Chau Yuen, Rui Zhang, Marco Di Renzo, and Merouane Debbah. 2020. Holographic MIMO surfaces for 6G wireless networks: Opportunities, challenges, and trends. *IEEE Wireless Communications* 27, 5 (2020), 118–125.

[26] Yi Huang and Kevin Boyle. 2008. *Antennas: from theory to practice.* John Wiley & Sons.

[27] Ruey Bing Hwang. 2000. Scattering characteristics of two-dimensionally periodic impedance surface. *IEEE Transactions on Antennas and Propagation* 48, 10 (2000), 1521–1527.

[28] Robert W. Heath Jr. 2019. Going Toward 6G [From the Editor]. *IEEE Signal Process. Mag.* 36, 3 (2019).

[29] KEYCOM. 2021. Frequency change Method, Free Space Type Dielectric Constant, Dielectric Loss Tangent, Transmission attenuation (Permittivity, Dk/Df) Measurement equipment. https://www.keycom.co.jp/eproducts/dps/dps10/page.html.

[30] Mohammad Khalaj-Amirhosseini. 2020. Phase-only synthesis of planar arrays using autocorrelation matching method. *Wiley International Journal of RF and Microwave Computer-Aided Engineering* 30, 5 (2020), 22153.

[31] Wahab Khawaja, Ozgur Ozdemir, Yavuz Yapici, Fatih Erden, and Ismail Guvenc. 2020. Coverage Enhancement for NLOS mmWave Links Using Passive Reflectors. *IEEE Open Journal of the Communications Society* (2020).

[32] B Langen, G Lober, and W+ Herzig. 1994. Reflection and transmission behaviour of building materials at 60 GHz. In *In Proceedings of IEEE International Symposium on Personal, Indoor and Mobile Radio Communications, Wireless Networks-Catching the Mobile Future*.

[33] Jean-Jacques Laurin et al. 2013. Specular reflection analysis for off-specular reflectarray antennas. *IEEE transactions on antennas and propagation* 61, 7 (2013), 3575–3581.

[34] Wonwoo Lee, Semin Jo, Kanghyeok Lee, Hong Soo Park, Junhyuk Yang, Ha Young Hong, Changkun Park, Sun K Hong, and Hojin Lee. 2021. Single-layer phase gradient mmWave metasurface for incident angle independent focusing. *Scientific reports* 11, 1 (2021), 1–7.

[35] Zhuqi Li, Can Wu, Sigurd Wagner, James C Sturm, Naveen Verma, and Kyle Jamieson. 2021. REITS: Reflective Surface for Intelligent Transportation Systems. In *In Proceedings of ACM HotMobile*.

[36] Zhuqi Li, Yaxiong Xie, Longfei Shangguan, Rotman Ivan Zelaya, Jeremy Gummeson, Wenjun Hu, and Kyle Jamieson. 2019. Towards programming the radio environment with large arrays of inexpensive antennas. In *In Proceedings of USENIX NSDI*.

[37] John Nolan, Kun Qian, and Xinyu Zhang. 2021. RoS: Passive Smart Surface for Roadside-to-Vehicle Communication. In *In Proceedings of ACM SIGCOMM*.

[38] Andreas E Olk, Pierre EM Macchi, and David A Powell. 2020. High-efficiency refracting millimeter-wave metasurfaces. *IEEE Transactions on Antennas and Propagation* 68, 7 (2020), 5453–5462.

[39] Open Signal. 2020. Quantifying the mmWave 5G Experience in the US. https://www.opensignal.com/2021/04/28/quantifying-the-mmwave-5g-experience-in-the-us.

[40] James M Ortega and Werner C Rheinboldt. 2000. *Iterative solution of nonlinear equations in several variables.* SIAM.

[41] Jae-Yong Park, Wonil Seo, Sehoon Yoo, and Young-Ho Kim. 2017. Effect of Cu electroplating parameters on microvoid formation and high-speed shear strength in Sn-3.0 Ag-0.5 Cu/Cu joints. *Elsevier Journal of Alloys and Compounds* 724 (2017), 492–500.

[42] Zhangyou Peng, Linxiao Li, Miao Wang, Zhonghao Zhang, Qi Liu, Yang Liu, and Ruoran Liu. 2016. An Effective Coverage Scheme With Passive-Reflectors for Urban Millimeter-Wave Communication. *IEEE Antennas and Wireless Propagation Letters* 15 (2016), 398–401.

[43] Reza Rofougaran. 2021. 5G mmWave Mobility Powered by Movandi. https://www.youtube.com/watch?v=1FnWOHG64Gw.

[44] Miguel Ruphuy and Carlos E Saavedra. 2021. 3D printed millimeter-wave beam-steering reflector using dielectric fluids. *JOSA A* 38, 2 (2021), 237–244.

[45] Aman Samaiyar, Ahmed H Abdelrahman, and Dejan S Filipovic. 2018. Iterative Phase Correction Technique for Design of Non-Conventional Reflectarray Antennas. In *In Proceedings of IEEE AP-S/URSI*.

[46] Diptiranjan Samantaray and Somak Bhattacharyya. 2020. A gain-enhanced slotted patch antenna using metasurface as superstrate configuration. *IEEE Transactions on Antennas and Propagation* 68, 9 (2020), 6548–6556.

[47] B Schultz. 2013. 802.11 ad–WLAN at 60 GHz–A technology introduction. *Rohde & Schwarz* (2013).

[48] Virendra V Singh, Fernando Soto, Kevin Kaufmann, and Joseph Wang. 2015. Micromotor-based energy generation. *Angewandte Chemie* 127, 23 (2015), 7000–7003.

[49] Siradel. 2021. Vocano 5G: Propagation Modeling for 5G Network Planning. https://www.siradel.com/solutions/software/volcano-5g/.

[50] Elahe Soltanaghaei, Akarsh Prabhakara, Artur Balanuta, Matthew Anderson, Jan M Rabaey, Swarun Kumar, and Anthony Rowe. 2021. Millimetro: mmWave retro-reflective tags for accurate, long range localization. In *In Proceedings of ACM MobiCom*.

[51] Ylo E. Stahler. 1963. Corner Reflectors as Elements Passive Communication Satellites. *IEEE Transactions on Aerospace* 1, 2 (1963), 161–172.

[52] StrataSys. 2021. VeroClear. https://www.stratasys.com/materials/search/veroclear.

[53] 3D Systems. 2021. VisiJet M3 Crystal. https://www.3dsystems.com/materials/visijet-m3-crystal.

[54] Xin Tan, Zhi Sun, Dimitrios Koutsonikolas, and Josep M Jornet. 2018. Enabling indoor mobile millimeter-wave networks based on smart reflect-arrays. In *In Proceedings of IEEE INFOCOM*.

[55] Mac E Van Valkenburg. 2001. *Reference data for engineers: radio, electronics,*

computers and communications. Newnes.

[56] Hiroki Wakatsuchi, Sanghoon Kim, Jeremiah J Rushton, and Daniel F Sievenpiper. 2013. Waveform-dependent absorbing metasurfaces. *APS Physical review letters* 111, 24 (2013), 245501.

[57] Song Wang, Jingqi Huang, Xinyu Zhang, Hyoil Kim, and Sujit Dey. 2020. X-Array: Approximating Omnidirectional Millimeter-Wave Coverage Using an Array of Phased Arrays. In *Proceedings of the 26th ACM Annual International Conference on Mobile Computing and Networking (MobiCom)*.

[58] Galen Watts. 2015. A surface treatment for non-specular reflection. In *Proceedings of IEEE AP-S/URSI*.

[59] Teng Wei and Xinyu Zhang. 2017. Pose Information Assisted 60 GHz Networks: Towards Seamless Coverage and Mobility Support. In *In Proceedings of ACM MobiCom*.

[60] Teng Wei, Anfu Zhou, and Xinyu Zhang. 2017. Facilitating Robust 60 GHz Network Deployment by Sensing Ambient Reflectors. In *Proceedings of the 14th USENIX Conference on Networked Systems Design and Implementation (NSDI)*.

[61] Tim Williams. 2016. *EMC for product designers.* Newnes.

[62] Xi Xiong, Justin Chan, Ethan Yu, Nisha Kumari, Ardalan Amiri Sani, Changxi Zheng, and Xia Zhou. 2017. Customizing indoor wireless coverage via 3D-fabricated reflectors. In *In Proceedings of ACM BuildSys*.

[63] Huan Yi, Shi-Wei Qu, Kung-Bo Ng, Chi Hou Chan, and Xue Bai. 2015. 3-D printed millimeter-wave and terahertz lenses with fixed and frequency scanned beam. *IEEE Transactions on Antennas and Propagation* 64, 2 (2015), 442–449.

[64] R. Ivan Zelaya, William Sussman, Jeremy Gummeson, Kyle Jamieson, and Wenjun Hu. 2021. LAVA: Fine-Grained 3D Indoor Wireless Coverage for Small IoT Devices. In *In Proceedings of ACM SIGCOMM*.

[65] Hanting Zhao, Ya Shuang, Menglin Wei, Tie Jun Cui, Philipp Del Hougne, and Lianlin Li. 2020. Metasurface-assisted massive backscatter wireless communication with commodity Wi-Fi signals. *Nature communications* 11, 1 (2020), 1–10.

[66] Renjie Zhao, Timothy Woodford, Teng Wei, Kun Qian, and Xinyu Zhang. 2020. M-cube: A millimeter-wave massive MIMO software radio. In *Proceedings of ACM MobiCom*.